

Figure 2.12 (a) Graph of the singular values of the coefficient matrix \mathbf{A} of the numerical Neumann problem on a 10×10 grid. All λ_i are non-zero except the last one. (b) shows \mathbf{u}_{100} , the nullspace vector of \mathbf{E}^T defining the solvability or consistency condition for a solution through $\mathbf{u}_{100}^T \mathbf{y} = 0$. Plotted as mapped onto the two-dimensional spatial grid (r_x, r_y) with $\Delta x = \Delta y = 1$. The interpretation is that the sum of the influx through the boundaries and from interior sources must vanish. Note that corner derivatives differ from other boundary derivatives by $1/\sqrt{2}$. The corresponding \mathbf{v}_{100} is a constant, indeterminate with the information available, and not shown. (c) A source \mathbf{b} (a numerical delta function) is present, not satisfying the solvability condition $\mathbf{u}_{100}^T \mathbf{b} = 0$, because all boundary fluxes were set to vanish. (d) The particular SVD solution, $\tilde{\mathbf{x}}$, at rank $K = 99$. One confirms that $\mathbf{A}\tilde{\mathbf{x}} - \mathbf{b}$ is proportional to \mathbf{u}_{100} as the source is otherwise inconsistent with no flux boundary conditions. With \mathbf{b} a Kronecker delta function at one grid point, this solution is a numerical Green function for the Neumann problem and insulating boundary conditions.

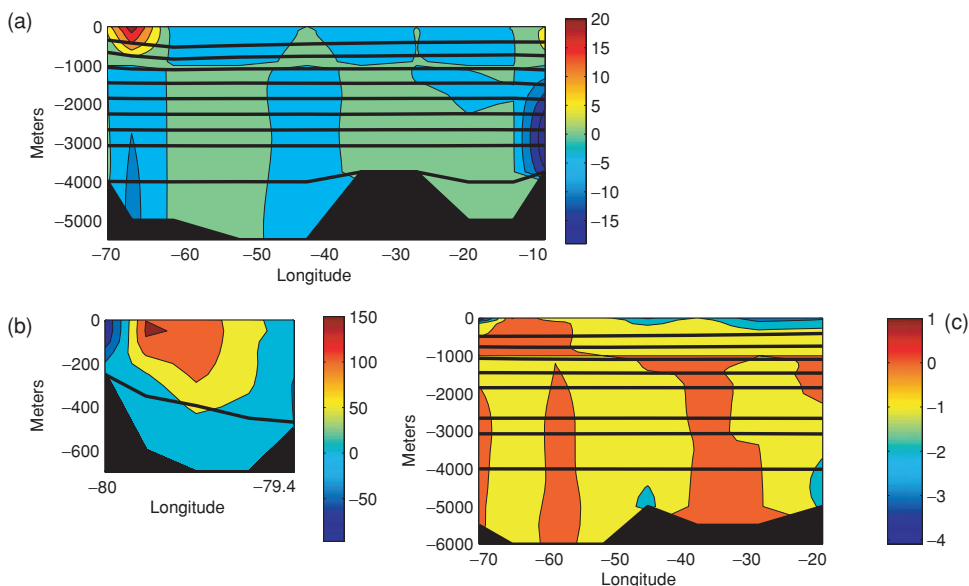


Figure 6.2 Geostrophic velocity (colors, in cm/s) relative to a 1000-decibar reference level, or the bottom, whichever is shallower, and isopycnal surfaces (thick lines) used to define ten layers in the constraints. Part (a) is for 36° N, (b) for the Florida Straits, and (c) for 24° N east of the Florida Straits. Levels-of-no-motion corresponding to the initial calculation are visible at 1000 m in the deep sections, but lie at the bottom in the Florida Straits. Note the greatly varying longitude, depth, and velocity scales.

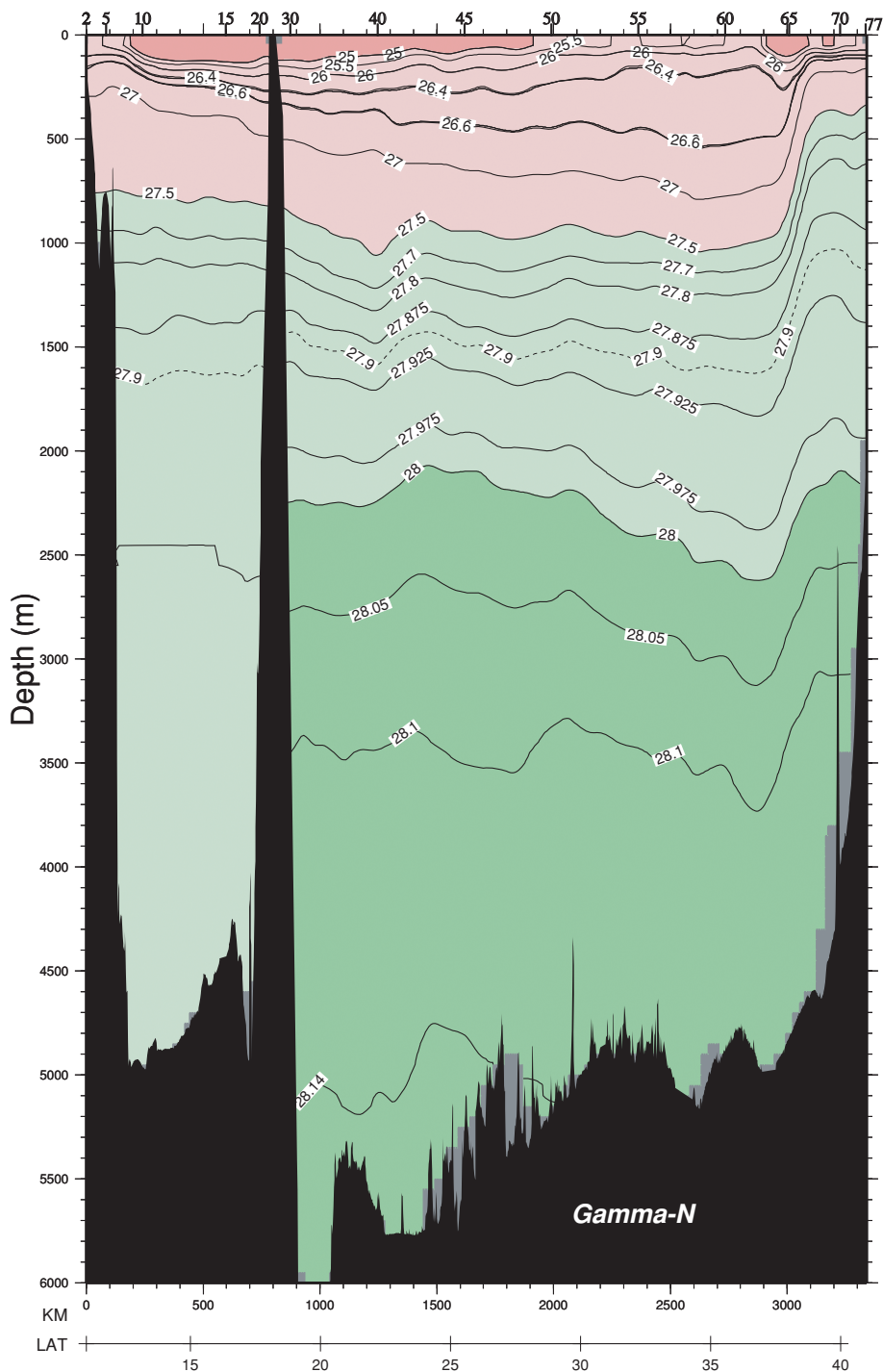


Figure 6.17 Density field constructed from the measurements at the positions in Fig. 6.16. Technically, these contours are of so-called neutral density, but for present purposes they are indistinguishable from the potential density.

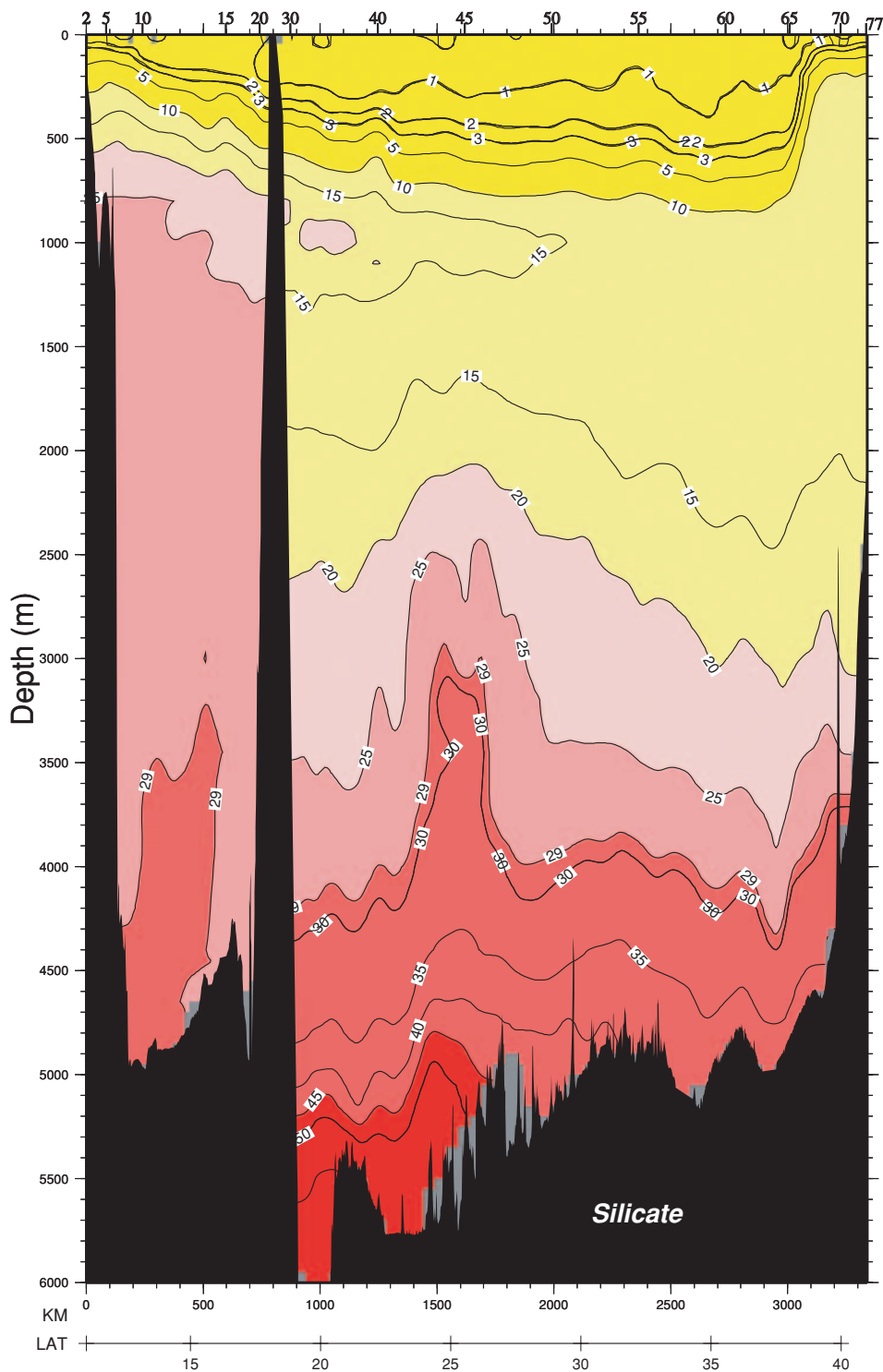


Figure 6.18 Same as Fig. 6.17, except showing the silicate concentration – a passive tracer – in μ moles/kg.

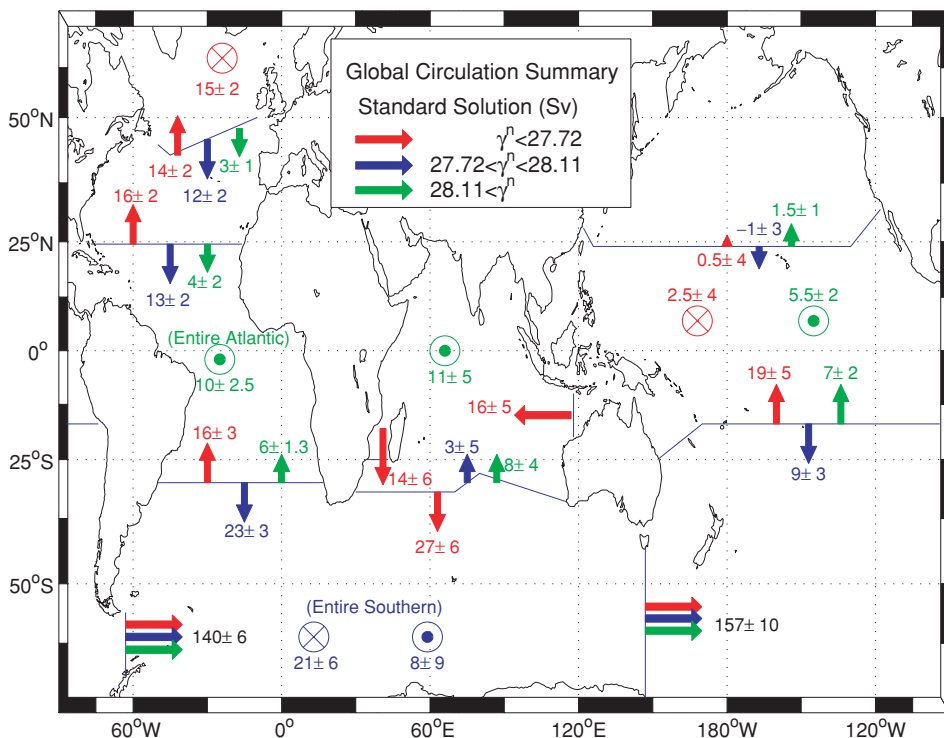


Figure 6.24 Mass flux in the Ganachaud (2003a) solution. Red, blue, and green arrows depict the vertically and horizontally averaged mass flux between the neutral surfaces noted. (Source: Ganachaud, 2003a)

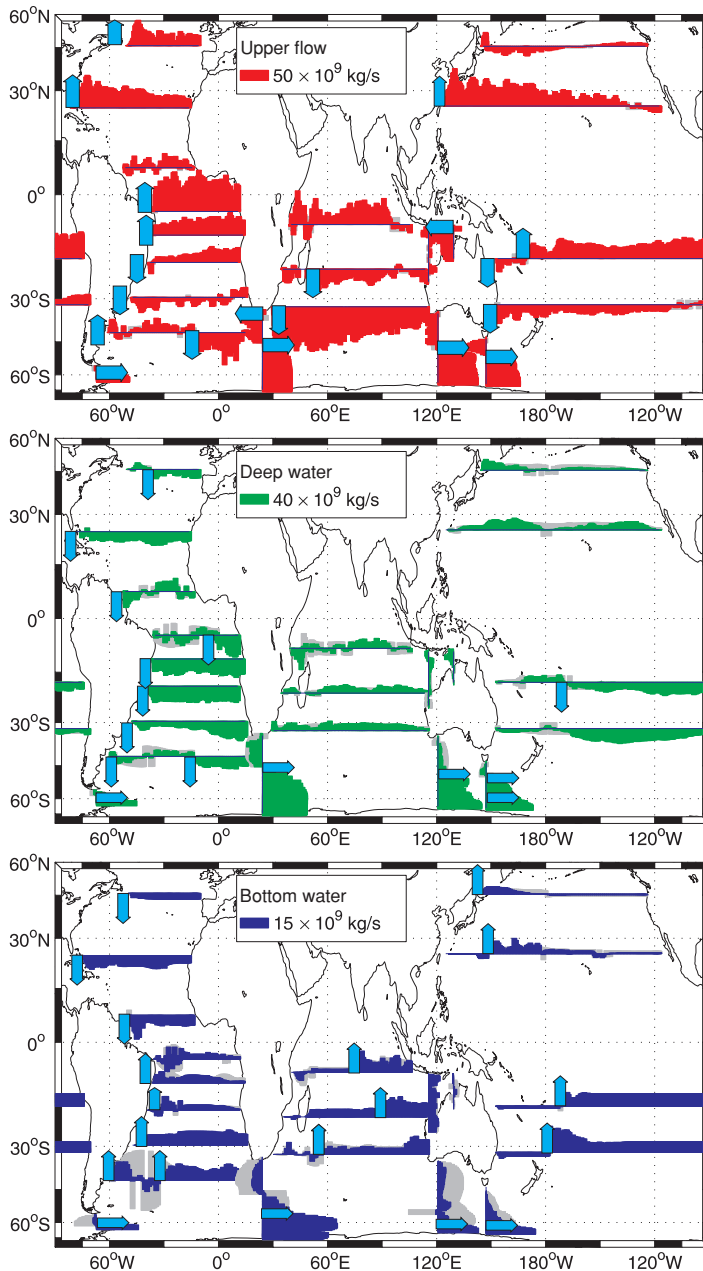


Figure 6.25 Mass transports integrated from west to east and north to south for the solution displayed in Fig. 6.24. Light shading shows the estimated standard errors. Arrows denote the major currents of the system. (Source: Ganachaud, 2003a)

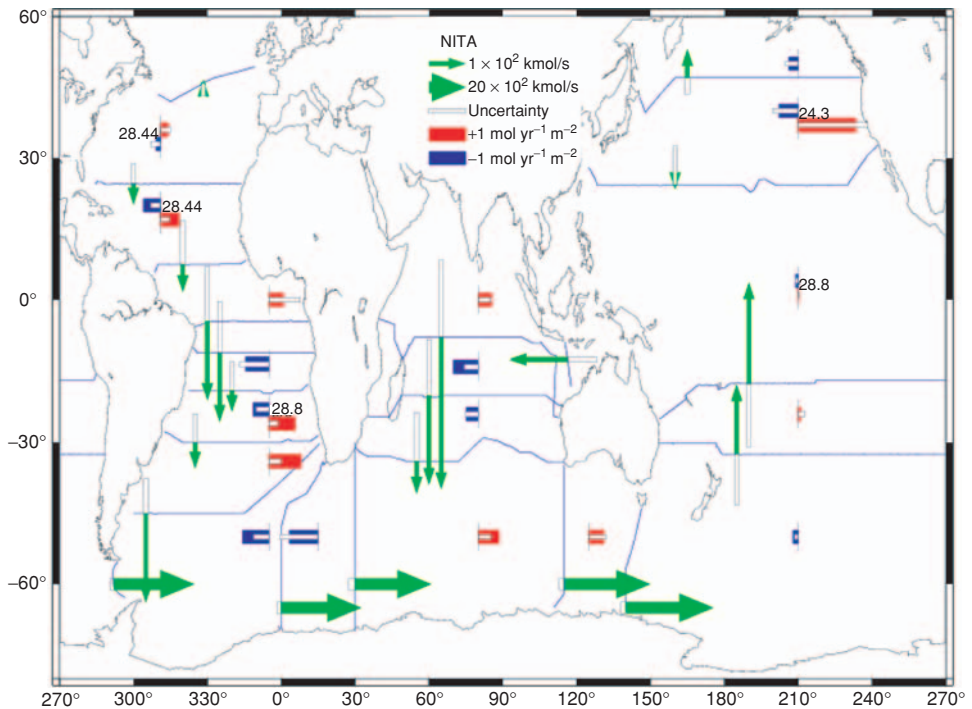


Figure 6.26 Integrated nitrate flux corresponding to the mass flux in Figs. 6.24 and 6.25. Although there is some resemblance to the mass fluxes, significant differences in the net movement of nitrate occur – owing to the spatially varying concentration of nitrate.

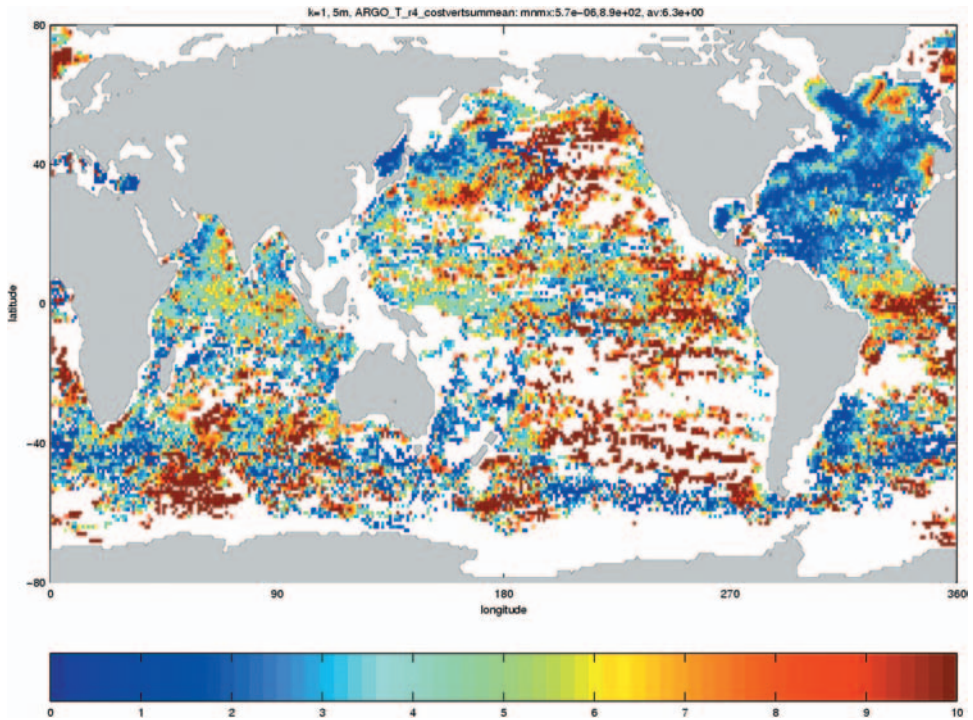


Figure 7.2 Misfit to so-called ARGO float temperature profiles. These instruments produce a vertical profile of temperature in the ocean above about 2000 m at pre-determined intervals (of order 10 days). The misfits shown here are weighted by the estimated errors in both model and data, and then averaged over the entire water column.

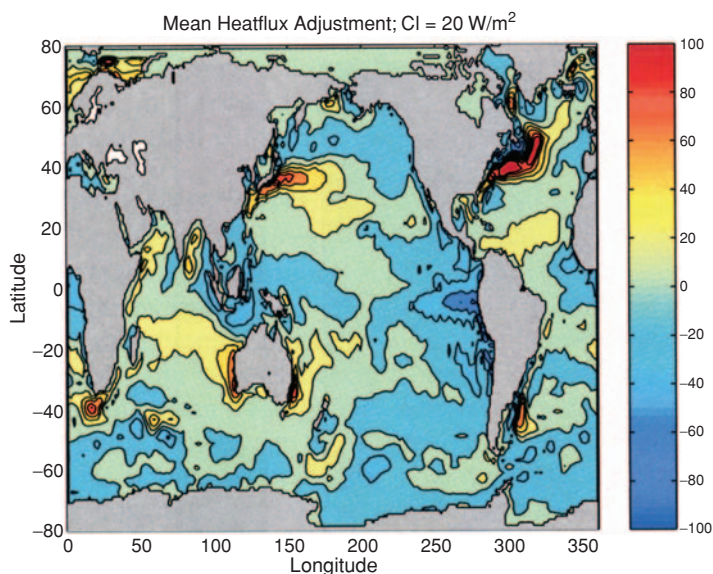


Figure 7.3 Mean changes in (a) net surface heat exchange (W/m^2), determined from six years of meteorological estimates and an ocean model. (Source: Stammer *et al.*, 2002)

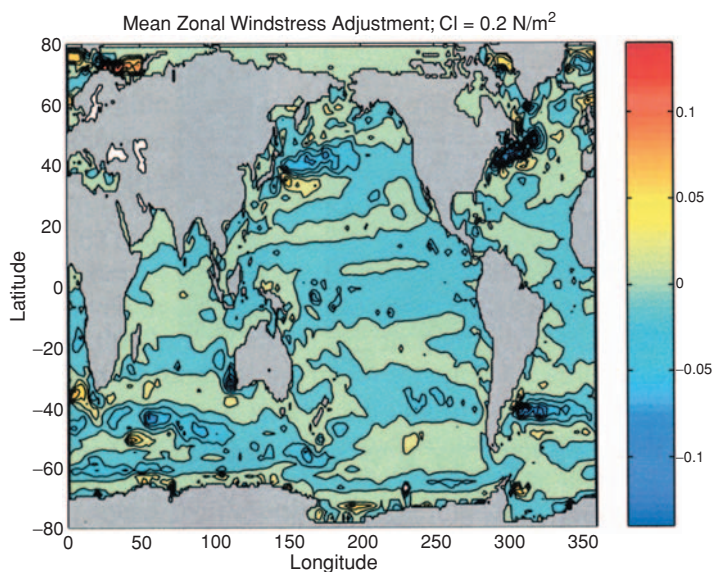


Figure 7.4 Adjusted wind stress (part of the control vector) in N/m^2 . (Source: Stammer *et al.*, 2002)

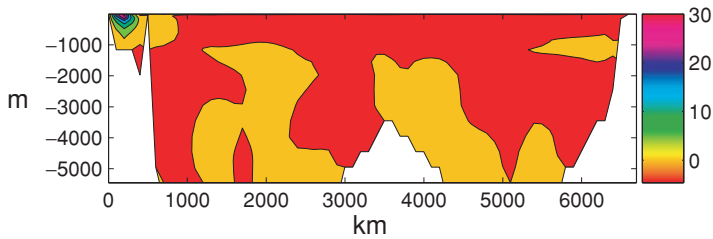


Figure 7.6 Twelve-year mean velocity across the North Atlantic Ocean (cm/s) at 26° N from a 13-year optimization of a 1 degree horizontal resolution (23 vertical layers) general circulation model and a large global data set. Red region is moving southward, remaining regions are all moving northward. Note the absence (recall Chapter 6) of any obvious level-of-no-motion, although there is a region of weak mean meridional flow near 1100 m depth. The northward-flowing Gulf Stream is visible on the extreme western side.

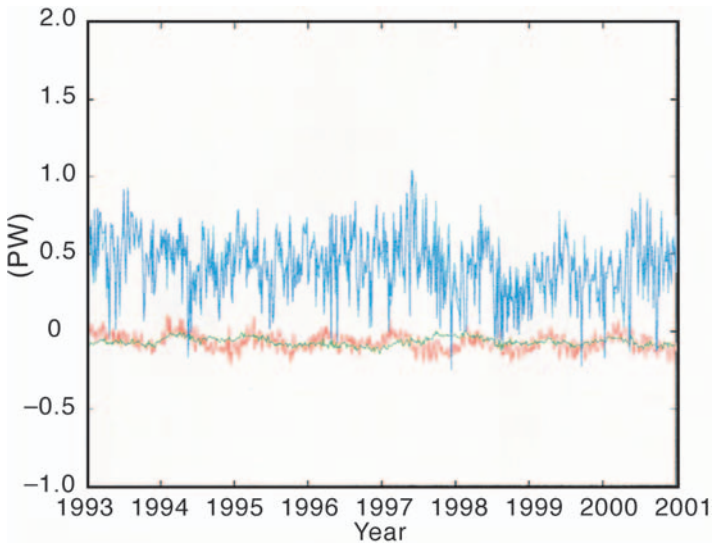


Figure 7.7 Time dependence in components of the meridional flux of heat across 21° S, in this case from eight years of analysis. The different colors correspond to different spatial integrals of the heat budget. (Source: Stammer *et al.*, 2003, Fig. 14)

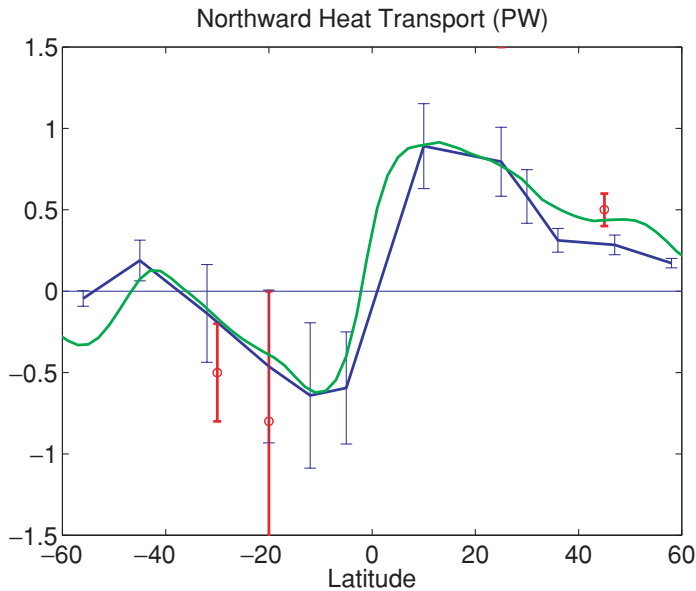


Figure 7.8 The blue curve shows the time and zonally integrated global meridional flux of heat (enthalpy) in the constrained model. The green curve shows the same field, estimated instead by integrating the fluxes through the surface. The two curves differ because heat entering from the surface can be stored rather than necessarily simply transported. Red bars are from the calculation of Ganachaud and Wunsch (2000) described in Chapter 6. Blue bars are the temporal standard deviation of the model heat flux and are an incomplete rendering of the uncertainty of the model result. (Source: Stammer *et al.*, 2003)

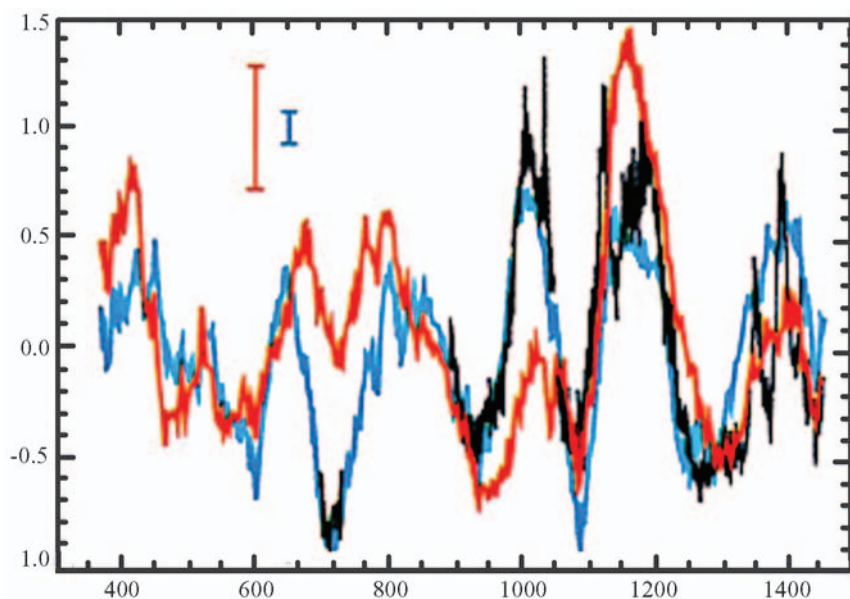


Figure 7.10 Comparison of temperature at 200 m depth at 8° N, 180° E of data (black), unconstrained model (red) and model constrained using altimetric data (blue). See Fukumori *et al.* (1999) for details and further comparisons. An approximate filter/smooth combination was used. (Source: Fukumori *et al.*, 1999)